Journal Name

ROYAL SOCIETY OF CHEMISTRY View Article Online
DOI: 10.1039/C9NJ04975D

ARTICLE

Diethylaminophenyl-based Schiff base Cu(II) and V(IV) complexes: experimental and theoretical study and cytotoxicity assays

Received 00th January 20xx,
Accepted 00th January 20xx

DOI: 10.1039/x0xx00000x

www.rsc.org/

Mariana Rocha[a], María C. Ruiz[b], Gustavo A. Echeverría[c,d], Oscar E. Piro[c,d], Ana L. Di Virgilio[b,d], Ignacio E. León[b,d], Antonio Frontera[e],* and Diego M. Gil[a,d,*]

A N,N,O,O donor Schiff base blocking ligand, [H_2L = 6,6'-((1*E*,1'*E*)-(ethane-1,2-diylbis(azaneylylidene))bis(methaneylylidene))bis(3-(diethylamino)phenol)), ***1***] has been used to synthesize mononuclear *[CuL]·H_2O* (***2***) and *[VO(L)]* (***3***) complexes. The ligand and complexes have been characterized by elemental, spectral (FTIR and UV-Vis) and thermogravimetric analysis. The molecular structures of (***1***) and (***2***) have been confirmed by single crystal X-ray diffraction studies. The crystal structure of the ligand (***1***) indicates that the molecule is sited on a crystallographic inversion centre and the planar conformation of the salicylideneimine moiety is favored by two intramolecular O-H···N1 hydrogen bonds forming S(6) ring motifs. Copper(II) center in complex ***2*** is coordinated in square planar fashion. The presence of an extended π-system in the complex (two chelate rings and two phenyl rings) facilitates the formation of chelate ring (CR)···π non-covalent interactions. DFT calculations have been performed to explore the energetic features of unconventional CR···π and hydrogen bonding interactions that are observed and described in the solid state of ***2***. Moreover, we have studied how the energy of the CR···π interaction is influenced by the substituent of the phenyl ring. In addition, the cytotoxic effect of the compounds has been tested against MG-63 (human osteosarcoma), HT-29 (human colorectal) and MCF7 (breast) cancer cell lines using the 3-(4,5-dimethylthiazol-2-yl)-2,5-diphenyltetrazolium bromide (MTT) assay.

.

1. Introduction

The interaction energy of conventional π–πstacking interactions is weak[1] (around 2 kcal/mol for the benzene dimer) compared to hydrogen bonding (6.9 kcal/mol for water-ammonia).[2] However, both are extremely important in biological systems as exemplified by nucleic acids where the double strand is formed due to a combination of H-bonds and π–π stacking interactions.[3] In addition, π–π stacking of aromatic systems are also used to explain a variety of physico-chemical phenomena, including spectroscopic properties, light harvesting,[4] and electron/hole transport in organic electronics.[5] In addition to the conventional π–π stacking-interactions[6] between aromatic rings, other more "unconventional" interactions have attracted the attention of the scientific community that embrace chelate ring stacking interactions involving transition and main group metals.[7-11] These interactions are important players in crystal engineering and metal–organic crystal structure formation.[12-14]

Schiff bases and their metal complexes have useful properties in different fields, ranging from biochemistry to industrial processes.[15] The chemistry and potential biological properties of Salen and Salophen Schiff bases and their metal complexes have been investigated extensively.[16-18] The most popular family of Schiff base ligands used in coordination chemistry is that derived from the coupling of aliphatic or aromatic diamines with phenolic aldehydes. Schiff bases have received much attention in a wide variety of fields due to their different applications owing to their characteristic properties such as preparative, accessibility, structural variety and varied coordinating ability. It is well known that the azomethine (-C=N-) linkage is responsible for the biological activities of Schiff bases including antitumor, antibacterial, antifungal, antioxidant, herbicidal and anti-VIH activities.[19-22] Metal complexes with Schiff bases as ligands have played an important role in the field of coordination chemistry due to their easy preparation, structural variety and biological properties. Recently, Rahman and co-workers have synthesized a new Salophen Schiff base that exhibited higher

[a] *INQUINOA (CONICET-UNT). Instituto de Química Orgánica. Facultad de Bioquímica, Química y Farmacia. Universidad Nacional de Tucumán. Ayacucho 471. T4000INI. San Miguel de Tucumán. Argentina. E-mail: dmgil@fbqf.unt.edu.ar*
[b] *CEQUINOR (CONICET-UNLP). Facultad de Ciencias Exactas. Universidad Nacional de la Plata. Bv. 120 Nº 1465. 1900. La Plata. Argentina.*
[c] *Departamento de Física. Facultad de Ciencias Exactas. Universidad Nacional de La Plata e IFLP (CONICET, CCT-La Plata). C.C. 67. 1900. La Plata. Argentina.*
[d] *Members of the Research Career of CONICET*
[e] *Department of Chemistry, Universitat de les Illes Balears, Crta de Valldemossa km 7.7, 07122 Palma de Mallorca (Baleares), SPAIN. E-mail: toni.frontera@uib.es*
*CCDC deposition numbers 1913605-1913608 contain the supplementary crystallographic data for compounds **1–4**.*

sensitivity and selectivity towards Sb^{3+} in the presence of other interfering heavy metal cations.[23]

In this contribution, we aim to explore and explain the crucial role of unconventional (chelate ring) π···π and H-bonding interactions in the self-assembly of a new copper(II) complex. We have synthesized and X-ray characterized a N_2O_2 donor Schiff base blocking ligand, H_2L = 6,6'-((1*E*,1'*E*)-(ethane-1,2-diylbis(azaneylylidene))bis(methaneylylidene))bis(3 (diethylamino)phenol) (*Scheme 1*) and we have used it to synthesize a mononuclear copper(II) complex. The crystal structure of both ligand and complex have been solved by single-crystal X-ray diffraction analysis. The noncovalent interactions have been studied and analyzed using Hirshfeld surface analysis, DFT calculations (M06-2X/def2-TZVP) and characterized by means of the NCI plot calculations. In addition, antitumoral properties have been evaluated for the free ligand and complexes to explore their cytotoxic capacity.

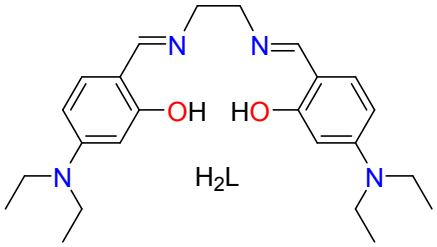

Scheme 1 Schematic representation of the ligand used in the work

2. Experimental Section

2.1. Materials

All reagents used in this work were obtained from Sigma Aldrich and used as received without further purification. Elemental (C, N, H) analysis were carried out using a Carlo Erba analyser. The solid state absorption IR spectra were recorded on a a FTIR Perkin Elmer GX1 in the 4000-400 cm^{-1} frequency range with spectral resolution of 4 cm^{-1}. The diffuse-reflectance UV-Vis spectra were recorded using a Shimadzu UV-2600 Spectrophotometer, using $BaSO_4$ as reference. Thermogravimetric studies were carried out between 25 and 800 ^oC in air flow using a Shimadzu TGA-50 thermobalance at a heating rate of 5 ^{o}/min. Room temperature magnetic susceptibility was measured on a magnetic susceptibility balance MSB-Auto and diamagnetic corrections were performed using Pascal's constants.

2.2. Synthesis

2.2.1 Synthesis of the Schiff base ligand H_2L (1).

The Schiff base ligand (H_2L) has been prepared by the condensation of 4-(diethylamino)salicylaldehyde (4 mmol) and ethylendiamine (2 mmol) in methanol. The resulting mixture was refluxed for 6 hours and allowed to cool at room temperature. After evaporation of the solvent, yellow colored solid product appeared of the desired ligand. Single crystals, suitable for X-ray diffraction, have been obtained after 2 days on slow evaporation of this solution in open atmosphere.

Yield: 68 %. Anal. Calc. For $C_{24}H_{34}N_4O_2$: C, 70.15; H, 8.28; N, 13.64 %. Found: C, 70.25; H, 8.30; N, 13.71 %.

2.2.2 Synthesis of complex [CuL]·H_2O(2).

1 mmol (0.411 g) of the Schiff base ligand (**H_2L**) was dissolved in 10 mL of methanol and 1 mmol (0.200 g) of $Cu(CH_3CO_2)_2{\cdot}H_2O$ in 10 mL of methanol was added in a drop wise manner with continuous stirring. The resulting mixture was refluxed for 4 hours to give a brown powder. The solution was filtered and the solid was recrystallized from hot methanol. Deep brown crystals suitable for X-ray data collection were obtained from slow evaporation of the solvent.

Yield: 85 %. Anal. Calc. For $C_{24}H_{34}N_4O_3Cu$: C, 58.76; H, 6.93; N, 11.43 %. Found: C, 58.67; H, 6.95; N, 11.51 %.

2.2.3. Synthesis of complex VOL (3).

1 mmol (0.411 g) of the Schiff base ligand (H_2L) was dissolved in 10 mL of methanol and then 1 mmol (0.265 g) of $VO(acac)_2$ in 10 mL of methanol was added to it. The resulting mixture was refluxed for 2 hours. The resulting green precipitate was filtered, washed with methanol and dried in air.

Yield: 78 %. Anal. Calc. for $C_{24}H_{32}N_4O_3V$: C, 60.32; H, 6.70; N, 11.73 %. Found: C, 60.41; H, 6.75; N, 11.69 %.

2.3. X-ray diffraction data and structure refinement

The measurements were performed on an Oxford Xcalibur Gemini, Eos CCD diffractometer with graphite-monochromated MoKα (λ = 0.71073 Å) radiation. X-ray diffraction intensities were collected (ω scans with ϑ and κ-offsets), integrated and scaled with CrysAlisPro[24] suite of programs. The unit cell parameters were obtained by least-squares refinement (based on the angular setting for all collected reflections with intensities larger than seven times the standard deviation of measurement errors) using CrysAlisPro. Data were corrected empirically for absorption employing the multi-scan method implemented in CrysAlisPro. The structures were solved by intrinsic phasing with SHELXT[25] and the molecular models refined with SHELXL.[25]

H_2L (1): The hydrogen atoms were located in a difference Fourier map phased on the heavier atoms and refined at their found positions with isotropic displacement parameters. The methyl groups converged to staggered angular conformations.

[CuL]·H_2O (2): All hydrogen atoms but the one of the water molecule (sited at a crystallographic two-fold axis) were positioned stereo-chemically and refined with the riding model. The methyl groups were refined as rigid entities allowed to rotate around the corresponding C-CH_3 bonds such as to maximize the sum of the residual electron density at the calculated H-positions. They converged to staggered angular conformations. The independent water hydrogen was located in a Fourier difference map and refined at its found position with an isotropic displacement parameter equal to 1.2 times the one of the water oxygen and Ow-H and H···H distances

View Article Online DOI: 10.1039/C9NJ04975D

restrained to target values of 0.86(1) and 1.36(1) Å, respectively.

Crystal data and structure refinement results are summarized in **Table 1**. Crystallographic structural data have been deposited at the Cambridge Crystallographic Data Centre (CCDC). Enquiries for data can be direct to: Cambridge Crystallographic Data Centre, 12 Union Road, Cambridge, UK, CB2 1EZ or (e-mail) deposit@ccdc.cam.ac.uk or (fax) +44 (0) 1223 336033. Any request to the Cambridge Crystallographic Data Centre for this material should quote the full literature citation and the reference number CCDC 1938493 for (***1***) and 1938494 for (***2***).

Table 1: Crystal data and structure refinement for compounds (***1***) and (***2***).

	1	***2***
Empirical formula	$C_{24}H_{34}N_4O_2$	$C_{24}H_{34}CuN_4O_3$
Molar mass	410.55	490.09
Temperature (K)	293(2)	293(2)
Wavelength (Å)	0.71073	0.71073
Crystal system	Triclinic	Monoclinic
Space group	*P -1*	*C 2/c*
Unit cell dimensions	a = 6.0163(5) Å b = 7.4951(5) Å c = 13.488(1) Å α = 105.570(6)° β = 100.446(7)° γ = 93.766(6)°	a = 19.5737(8) Å b = 9.8513(4) Å c = 12.4452(4) Å β = 93.654(3) º
Volume (Å^3)	571.97(8)	2394.9(2)
Z	1	4
Density, calculated (Mg/m^3)	1.192	1.359
Absorption coefficient (mm^{-1})	0.077	0.944
F(000)	222	1036
θ-range for data collection (º)	3.469 to 28.804	3.281 to 28.867
Index ranges	-7≤h≤ 7, -9≤ k≤ 9, -17 ≤ l ≤ 16	-26≤ h ≤ 25, -8 ≤ k≤13, -16≤ l ≤15
Reflections collected	4408	4950
Independent reflections	2446 [R(int)= 0.0245]	2575 [R(int)= 0.0190]
Observed reflections [I>2σ(I)]	1408	2273
Completeness to ϑ = 25.242° (%)	99.8	99.8
Refinement method	Full-matrix least-squares on F^2	Full-matrix least-squares on F^2
Data / restrains / parameters	2446 / 0 / 204	2575 / 2 / 152
Goodness-of-fit on F^2	1.022	1.033
Final R indices[a] [I>2σ(I)]	R1 = 0.0537, wR2 = 0.1115	R1 = 0.0403, wR2 = 0.1029
R indices (all data)	R1 = 0.0994, wR2 = 0.1403	R1 = 0.0471, wR2 = 0.1093
Largest diff. peak and hole (e.Å^{-3})	0.103 and -0.139	0.745 and -0.279

[a] $R_1=\Sigma||F_o|-|F_c||/\Sigma|F_o|$, $wR_2=[\Sigma w(|F_o|^2-|F_c|^2)^2/\Sigma w(|F_o|^2)^2]^{1/2}$

2.4. Hirshfeld surface calculations

An analysis of the Hirshfeld surfaces and the corresponding 2D fingerprint plots (full and decomposed)[26] was carried out employing *CrystalExplorer*3.0[27] program to visualize and quantify different molecular interactions. The Hirshfeld surfaces were mapped over d_{norm} and shape index properties. The d_{norm} property is a symmetric function of distances to the surface from nuclei inside and outside the Hirshfeld surface (*d*i and *d*e, respectively), relative to their respective van der Waals radii. The regions with red and blue color on the d_{norm} represent the shorter and longer inter contacts; the white color indicates the contacts around the van der Waals radii. The d_{norm} surface was mapped with color scale in the range –0.020 au (blue) to 0.750 au (red) and shape index mapped in the color range of -1.00 au (concave) and 1.00au (convex). The 2D fingerprint plots (*d*i *vs* *d*e) were displayed using the expanded 0.6–2.8 Å range.

2.5. Theoretical Methods

The calculations of the non-covalent interactions were carried out using the Gaussian09[28] and the M06-2X/def2-TZVP level of theory. The crystallographic coordinates have been used to evaluate the interactions in the solid state. This procedure and level of theory have been successfully used to evaluate similar interactions.[29] We have not fully optimized the assemblies because we are interested in the calculation of the contribution of each interaction using the geometry they have in the X-ray structure. It is not the purpose of this study to obtain the most energetically favourable orientation of the components of the assembly. The interaction energies were computed by calculating the difference between the energies of isolated monomers and their assembly. The interaction energies have been calculated with correction for the basis set superposition error (BSSE) by using the Boys–Bernardi counterpoise technique.[30] The molecular electrostatic potential surfaces have been computed using the Gaussian09 software at the M06-2X/def2-TZVP.

The NCI plot[31] iso-surfaces have been used to characterize noncovalent interactions. They correspond to both favourable and unfavourable interactions, as differentiated by the sign of the second density Hessian eigenvalue and defined by the isosurface color. The color scheme is a red-yellow-green-blue scale with red for ρ^+_{cut} (repulsive) and blue for ρ^-_{cut} (attractive). Yellow and green color indicate weak repulsive and weak attractive interactions, respectively.[32] The Gaussian09 B3LYP-D/6-31+G* level of theory wave function has been used to generate the NCI plot.

2.6. Cell line and growth conditions

Human osteosarcoma cell line (MG-63), human colorectal cancer cell line (HT-29), and a breast cancer cell line (MCF7) were grown in Dulbecco's modified Eagle's medium (DMEM) containing 10% fetal bovine serum (FBS), 100 IU/mL penicillin and 100 µg/mL streptomycin at 37 °C in 5% CO2 atmosphere. Breast cancer cell line (MDA-MB-231), was grown in DMEM-F12, in the same conditions. All cancer cell lines were grown in a 75 cm^2 flask until they reach 70–80% of confluence. Then, the cells were subcultured using TrypLE TM. For experiments,

cells were grown in multi-well plates. Dulbecco's modified Eagle's medium (DMEM), DMEM-F12 and TrypLE ™ were purchased from Gibco (Gaithersburg, MD, USA), and fetal bovine serum (FBS) was purchased from Internegocios (Argentina). Tissue culture materials were purchased from Corning (Princeton, NJ, USA).

2.7. Cell viability: 3-(4,5-Dimethylthiazol-2-yl)-2,5-diphenyltetrazolium bromide assay

The 3-(4,5-dimethylthiazol-2-yl)-2,5-diphenyltetrazolium bromide (MTT) assay was performed according to Mosmann.[33] Briefly, cells were seeded in a 96-well dish, allowed to attach for 24 h, and treated with different concentrations (1 to 100 µM) of the ligand **(*1*)**, or the complexes **(*2*)** or **(*3*)** at 37 ºC for 24 h. Afterward, the medium was changed and the cells were incubated with 0.5 mg/mL MTT under normal culture conditions for 3 h. Cell viability was marked by the conversion of the tetrazolium salt MTT to a coloured formazan by mitochondrial dehydrogenases. Colour development was measured spectrophotometrically with a microplate reader (multiplate reader multiskan FC, thermo scientific) at 570 nm after cell lysis in DMSO (100 µL per well). Cell viability was plotted as the percentage of the control value.

3. Results and Discussion

3.1. Synthesis

The tetradentate N_2O_2 donor Schiff base ligand (H_2L) has been produced by the condensation of ethylendiamine and 4-(diethylamino)-2-hydroxybenzaldehyde following the literature method.[34] Treatment of the tetradentate Schiff base ligand with the metal salts copper(II) acetate and $VO(acac)_2$ in a 1:1 molar ratio led to the formation of complexes *[CuL]·H₂O* (**2**) and *VOL* (***3***), respectively. Synthesis of compounds ***1*** and ***2*** is shown in *Scheme 2*. Values of magnetic susceptibility (μ_B) for complexes **2** and **3** are 1.82 and 1.75 MB, respectively typical values for square planar Cu(II) and V(IV) monomeric complexes.

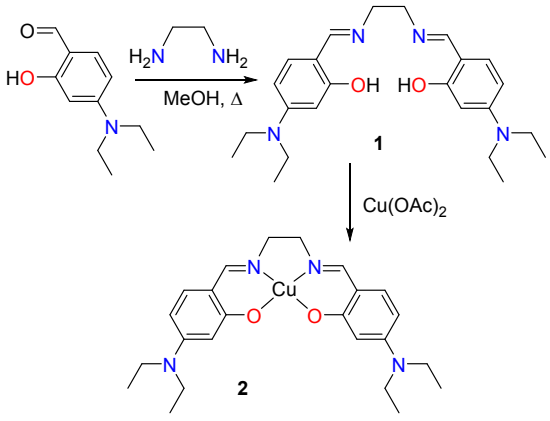

Scheme 2 Synthetic route to ligand ***1*** and complex ***2***.

3.2. IR and electronic spectra

The IR spectra of the free Schiff base ligand (H_2L) and its Cu(II) and VO(IV) complexes are given in Fig. S1, ESI†. The broad band at 3435 cm^{-1} in the IR spectrum of the free ligand is assigned to the O-H stretching mode corresponding to the phenolic hydroxyl group. The strong band observed at 1615 cm^{-1} is assigned to the C=N stretching mode and the medium intensity band at 1282 cm^{-1} is attributed to ν(C-O) vibration, which are characteristic bands of Schiff bases.[35] The coordination of the Schiff base to metal ions through the nitrogen atom is expected to reduce electron density in the imine link and lower the ν(C=N) absorption frequency. The IR spectra of show strong bands at 1591 cm^{-1} and 1587 cm^{-1} for complexes ***2*** and ***3***, respectively attributed to imine ν(C=N) stretching mode. In addition, the coordination of the phenolic groups with the metal ions can be examined by the ν(C-O) stretching mode, which is shifted to lower frequencies (1249 and 1250 cm^{-1} for complexes ***2*** and ***3***, respectively). The IR spectra of *[Cu(L)]·H₂O* exhibits additional weak bands at 526 and 477 cm^{-1}, which can be attributed to the ν(Cu-N) and ν(Cu-O) stretching modes, respectively. The V=O bond in VO(IV) complexes can be regarded as a multiple covalent bond, the π component consisting of pπ electrons to oxygen of dπ orbitals of vanadium. The electron-accepting capacity of VO(IV) markedly depends upon the ligands coordinated to the oxycation moiety. Depending upon the donor ability of ligand, by increasing the electron density in the metal, the O(pπ) → V(dπ) donation is reduced, lowering the V=O bond order and consequently decreasing the ν(V=O) frequency. In complex ***3***, the bands at 987 and 975 cm^{-1} are assigned to V=O stretching mode. The bands at 606 and 479 cm^{-1} are assigned to V-O and V-N stretching modes.

The electronic spectra of the Schiff base ligand *H_2L* and its *[Cu(L)]·H₂O* and *[VO(L)]* complexes were recorded within the range 200-800 nm in solid state (see Fig. S2, ESI†). The spectral band at 262 nm is assigned to π → π* transitions corresponding to the phenolic rings. The band located at 358 nm is attributed to n→π* transition of the azomethine moiety, while the bands at 375 and 546 nm are assigned to n→π* transitions of donating atoms like O or N which are overlapped with the intermolecular LCT from aromatic rings.[36] The bands related to the transitions involving the phenyl rings have been unaffected in the spectra of complexes. Moreover, the bands due to intraligand transitions (azomethine chromophore) are shifted to longer wavelengths, indicating that the imine N atoms is involved in the coordination to the metal centers. The electronic spectrum of complex (***2***) exhibits two bands at 479 and 561 nm attributed to $^2B_{1g} \rightarrow {}^2A_{1g}$ and $^2B_{1g} \rightarrow {}^2E_g$ electronic transitions, respectively. These transitions confirm the square planar geometry of complex (***2***), typical of Cu(II) complexes with Schiff bases.[36-38] The broad band observed in the spectrum of (***3***) between 550 and 700 nm are assigned to the *d-d* transition of the VO(IV) complex.

3.3. Description of crystal structures

3.3.1. H_2L (1)

The solid-state molecular structure of the Schiff base (***1***) is shown in Fig. 1. Selected bond lengths and angles are given in Table S1, ESI†. The molecule is sited on a crystallographic inversion centre. The planar conformation of the

salicylideneimine moiety is favoured by two intra-molecular O-H···N1 hydrogen bonds, which form S(6) ring motifs [O···N1 distance of 2.6016(2) Å]. According to this analysis, the H_2L ligand exists in the *phenol-imine* form, as shown in Fig. 1. The C2-O length is 1.359(2) Å, consistent with the single bond character of this link. The C7=N1 imine bond shows an *E* configuration with a bond length of 1.278(3) Å, as expected for a C=N double bond. The C8-N1-C7 bond angle of 119.1(2)º is consistent with the sp^2 hybrid character of N1 atom and the group has a C1-C7-N1-C8 torsion angle of -179.5(2)º. The bond lengths and angles within the benzene ring are in the range from 1.371(2) Å to 1.406(3) Å as expected for a resonant structure. The crystal of (***1***) is further stabilized by weak inter-molecular C8-H8B···O hydrogen bonds [d(H···O) = 2.684 Å], given rise to a layered structure parallel to (001) plane, as illustrated in Fig. S3, ESI†. These hydrogen bonds generate $R_2^2(16)$ ring motifs.

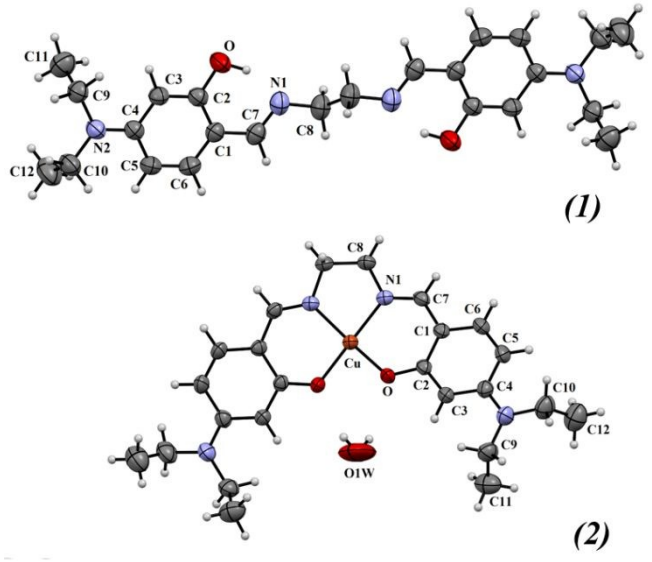

Fig. 1. ***Top*** X-ray structure of the ligand ***1*** showing the labels of the non-H atoms and their displacement ellipsoids at the 30% probability level. The unlabeled half of the molecule is obtained from the labeled one through a crystallographic inversion centre. ***Bottom***: Solid state molecular structure of complex ***2***. The left molecular half is symmetry related to the right half by a two-fold axis along the vertical.

3.3.2. [Cu(L)]·H_2O (2)

A view of *[Cu(L)]·H_2O* (**2**) complex is included in Fig. 1. The structural study reveals that the complex is hosted in the lattice as monomeric units having an approximately planar configuration around the central Cu(II) ion. The metal is in a square-planar environment, *cis* coordinated to two imine N atoms and two phenoxo O atoms from the deprotonated Schiff base ligand. Selected bond lengths and angles are given in Table 2. The C-N bond length is 1.291(3) Å, showing the expected lengthening of C=N double bond upon coordination to the metal. The Cu-N and Cu-O bond lengths are 1.936(2) and 1.917(2) Å, respectively. The observed geometry around the Cu(II) ion is confirmed by the τ_4 index,[39] which indicates the distortion between the perfect tetrahedron (τ_4 = 1.0) and a perfect square planar geometry (τ_4 = 0). The τ_4 value for the Cu(II) metal centre is 0.2301, indicating that the geometry is in fact distorted square planar. The distortion observed in the complex could in part be attributed to the presence of one water molecule which give rise to intra-molecular OW-H···O hydrogen bonds [d(H…O) = 2.39(5) Å]. Weak non-covalent interactions such as C-H···X (X= O, N, S, halogen) and π-stacking, also play significant roles in conformation, crystal packing supra-molecular assembly, and physico-chemical properties. Although there are no classical hydrogen bonds in the crystal structure of complex, two intermolecular C-H···O contacts are observed in the solid state. Intermolecular hydrogen bonds occur between C8-H8B···Ow [2.854 Å] (see Fig. S4, ESI†). Finally, the crystal packing of the complex presents self-assembled dimers, governed by (chelate ring) π···π stacking interactions (see Fig. S4, ESI†, Table 3). These dimers are formed between two neighbouring complexes in the lattice probably because the almost orthogonal arrangement of the phenyl ring (C1-C6, Cg4 centroid) with respect to the chelate ring (Cu/O/C2/C1/C7/N1, Cg3 and Cg2 centroids). This favors the interaction between the chelate and phenyl rings, with centroid-to-centroid distance of 3.5951(1) Å. The Cg2···Cg4^{i} and Cg3···Cg4^{ii} interactions [symmetry operations: (i) –x,-y,1-z; (ii) x, -y,-1/2+z] form centre-symmetric dimers and the corresponding pairs of main planes are close to parallel-displaced to each other, with inter-plane angles of 5º. This remarkable interaction is further discussed below.

Table 2: Selected bond lengths (Å) and angles (º) for the complex *[Cu(L)]·H_2O* (***2***).

Bond lengths		Angles	
Cu-N1#	1.9358(19)	O-Cu-N1	93.79(7)
N1-Cu	1.9358(19)	N1#-Cu-N1	83.74(11)
O-Cu	1.9173(16)	O-Cu-N1#	163.78(8)
Cu-O#	1.9173(16)	O-Cu-O#1	92.88(10)
N1-C7	1.291(3)	O1#-Cu-N1#1	93.79(7)
C2-O	1.320(3)	O1#-Cu-N1#	163.78(8)
N1-C8	1.466(3)	C7-N1-Cu	125.59(16)
		C8-N1-Cu	112.89(14)
		C2-O-Cu	126.88(15)

Symmetry transformations used to generate equivalent atoms: #1 –x+1,y,-z+1/2

Table 3 Geometrical parameters for the π-stacking moieties involved in the π···π interactions for complex *[Cu(L)]·H_2O* (***2***).

Cg(I)-Cg(J)[a]	d(Cg···Cg)[b]	α[c]	β[d]	γ[e]	Symmetry
Cg2···Cg4	3.5951(1)	5.0	22.7	27.6	-x,-y,1-z
Cg2···Cg3	3.6765(2)	0.0	26.8	26.8	x,-y,-1/2+z
Cg3···Cg4	3.5951(1)	5.0	22.7	27.6	x,-y,-1/2+z
Cg4···Cg4	4.9721(2)	0.0	50.9	50.9	-x,-y,1-z

[a]Cg2: centroid of Cu-O-C2-C1-C7-N1, Cg3: centroid of Cu-OA-C2A-C1A-C7A-N1A, Cg4: centroid of C1-C6. [b]Centroid-centroid distance (Å). [c]Dihedral angle between the mean planes I and J. [d]Angle between the centroid vector Cg(I)···Cg(J) and the normal to the plane (I). [e]Angle between the centroid vector Cg(I)···Cg(J) and the normal to the plane (J).

View Article Online
DOI: 10.1039/C9NJ04975D

3.4. Thermal analysis

Thermal analysis (TG) of the $[Cu(L)]\cdot H_2O$ and [VO(L)] complexes (Fig. 2) were used to obtain relevant information about the thermal stability of these new complexes as well as to verify the status of water molecules into inside or outside the inner coordination sphere of the metal centre.

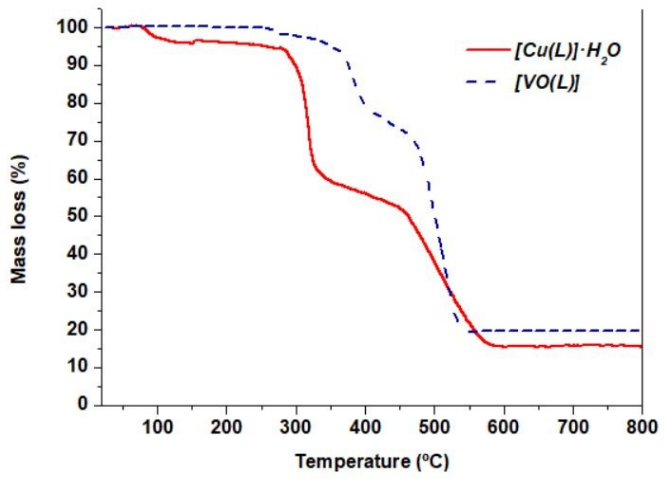

Fig. 2 TG curves for the thermal decomposition of complexes (***2***) and (***3***) in air.

The mass losses obtained from TG curves are in good agreement with the theoretical values. Complex (***2***) decomposed in three steps. The first decomposition step finishes at 108 ºC with a mass loss of 3.50% (theoretical value: 3.67%) and it is associated to the removal of one water molecule. The low temperature of the removal of water molecule indicates the non-coordinated character of this molecule. The next degradation steps represent the decomposition of the ligand and the remaining product at 600 ºC is identified as CuO by IR spectroscopy (observed mass loss: 83.43%, theoretical mass loss: 83.77%). For complex (***3***), no mass loss was observed until 250 ºC which confirm that the VO(IV) complex is anhydrous. The complex decomposes at temperatures higher than 250 ºC in two consecutive steps to form V_2O_5 oxide as final product from the complex (observed mass loss: 80.26%, calculated value: 80.95%).

3.5. Theoretical Study

A new copper(II) coordination complex has been synthesized and characterized by X-ray structure analysis (see Fig. 1). As described above this complex forms H-bonding and π-stacking interactions that are crucial for determining its solid state structure. The theoretical study has been devoted to analyse energetically both interactions. At first, the molecular electrostatic energy (MEP) surface has been computed to rationalize the interactions from an electrostatic point of view (see Fig. 3). The most electron rich region is located in the middle of both O-atoms (–67 kcal/mol) and the most positive region at H-atoms of the ethylene linker between the imino groups. This is likely due to the coordination of the iminic N-atoms to the metal centre, thus increasing the acidity of the H-atoms by inductive effect. Moreover, the MEP values over the phenyl and chelate rings are –30.0 and –10 kcal/mol, respectively. These MEP values anticipate the formation of antiparallel π-stacking interactions to minimize the electrostatic repulsion between the π-clouds.

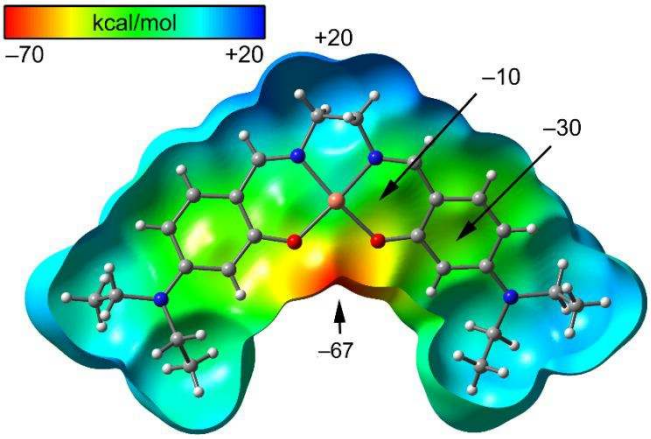

Fig. 3. Molecular electrostatic potential (MEP) surfaces of complex ***2***. The isosurface value is 0.001 a.u. The MEP energies at selected points have been indicated in kcal/mol.

In Fig. 4(a), a partial view of the solid state of complex ***2*** is shown highlighting the formation of an infinite supramolecular chain along the *c* direction as a consequence of the CR···π stacking interactions already described in Fig. S5, ESI†. A close examination of the stacking mode reveals that the chelate ring (in green) mainly interacts with the phenyl ring (in orange) to minimize electrostatic repulsion, in good agreement with the MEP analysis that shows negative MEP values over both six membered rings. The binding energy of one dimer extracted from the infinite chain has been computed (see Fig. 4b) and the interaction energy is ΔE_1 = –22.2 kcal/mol, that is very strong in agreement with previous calculations on CR···π interactions.[39-41] In order to evaluate the effect of the electron donating $–NEt_2$ substituent, we have computed an additional model where two $–NEt_2$ substituents have been replaced by H-atoms, (see Fig. 4c). As a result, the interaction energy is reduced to ΔE_2 = –19.4 kcal/mol, which is unexpected, since the elimination of the strong electron donating group should reduce the electrostatic repulsion of both π-clouds. A likely explanation is that the ethyl groups also participate in the formation of the assembly via van der Waals interactions. In fact, if the H-atoms are replaced by electron withdrawing cyano groups (see Fig. 4d, small arrows), the interaction energy becomes more favorable (compared to the model in Fig. 4c), ΔE_3 = –21.5 kcal/mol, thus confirming that the presence of electron withdrawing substituents reinforces the CR···π interaction.

View Article Online
DOI: 10.1039/C9NJ04975D

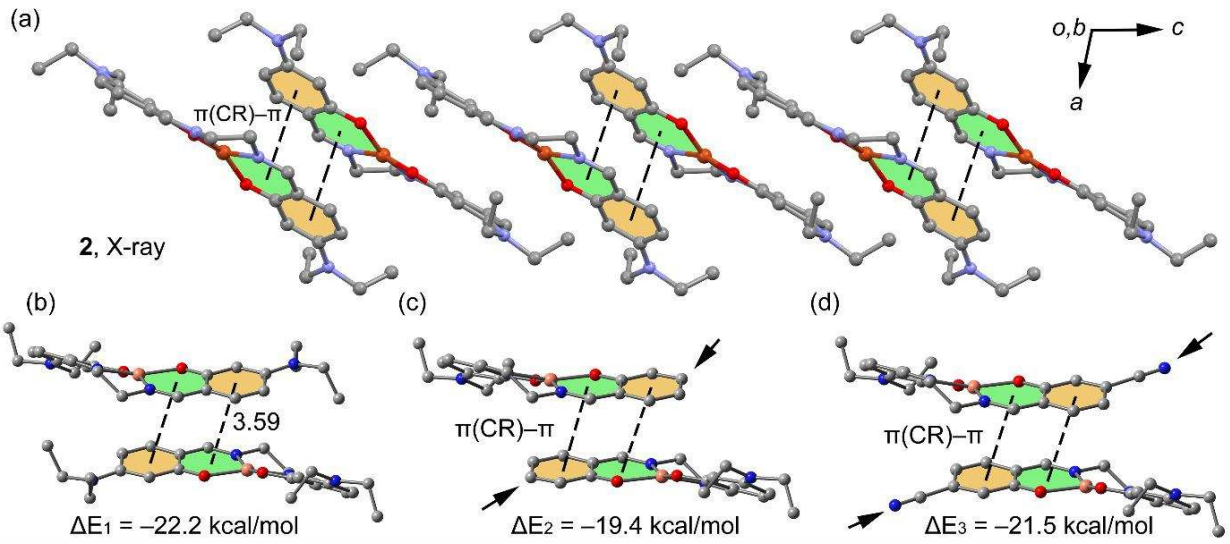

Fig. 4: (a) A section of the crystal structure (determined by X-ray structure analysis) of complex ***2***. **(b-d)** Theoretical models used to compute the binding energy. Distances in Å.

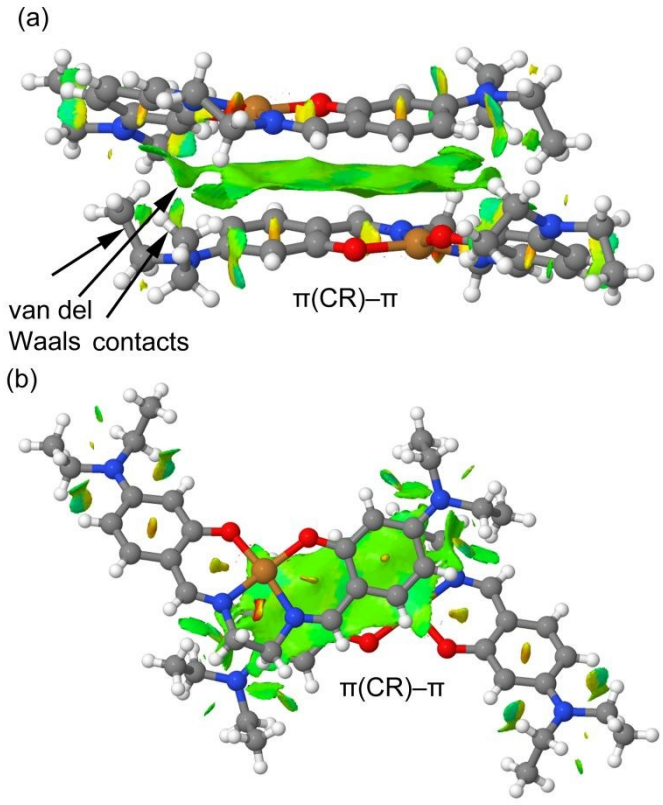

Fig. 5 Perspective **(a)** and on-top **(b)** NCI plots of the self-assembled CR···π dimer in ***2***. The gradient cut-off is s = 0.35 au, and the color scale is $-0.04 < \rho < 0.04$ au.

With the purpose to further analyse and characterize the CR···π interactions commented described in Fig. 4, we have used the NCI plot index computational tool. This tool allows to visualize and identify the non-covalent interactions efficiently and also the extent to which weak interactions stabilize a complex. **Fig. 5** shows the NCI plot (two views) obtained for the CR···π self-assembled dimer. It can be observed the presence of an extended and green isosurface that is located between the chelate and aromatic rings confirming the existence of the CR···π interactions. The on-top representation (see Fig. 5b) clearly shows that the surface embraces both chelate ring (including the metal centre) and the aromatic rings, thus explaining the large interaction energy obtained for this dimer. The NCI plot also shows the presence of small green isosurfaces located between the ethyl groups, thus confirming the existence of van der Waals interactions in this dimer of compound **2**.

In Fig. 6(a), we have represented another supramolecular chain that propagates in the *b* direction of the crystal structure of complex ***2***. In this supramolecular chain, the water molecules link the Cu-complexes by establishing two H-bonds as donor and two H-bonds as acceptor. This agrees well with the aforementioned MEP surface analysis, which revealed that the most electron rich region is located at the O-atoms and the most positive at the H-atoms of the ethylene linker. The binding energy of the dimer where the water molecule acts as H-bond donor (see Fig. 6b) is ΔE_4 = –8.0 kcal/mol, which falls in the typical range of H-bonding interactions.[42] For the other dimer, where the water acts as H-bond acceptor (Fig. 6c), the strength of the interaction is weaker ΔE_5 = –2.3 kcal/mol, due to the fact that the H-bond donor is a C–H group instead of a O–H group and the longer H···O distance. We have further characterized these H-bonds using the NCI plot index computational tool (Fig. 6d) and it can be observed the presence of two small and bluish isosurfaces located between the H-atoms of water and the O-atoms confirming the existence and attractive nature of the O–H···O interactions. The C–H···O H-bonds are characterized by a more extended green isosurface located between the O atom of water and the H-atoms of the $–CH_2–CH_2–$ linker.

View Article Online
DOI: 10.1039/C9NJ04975D

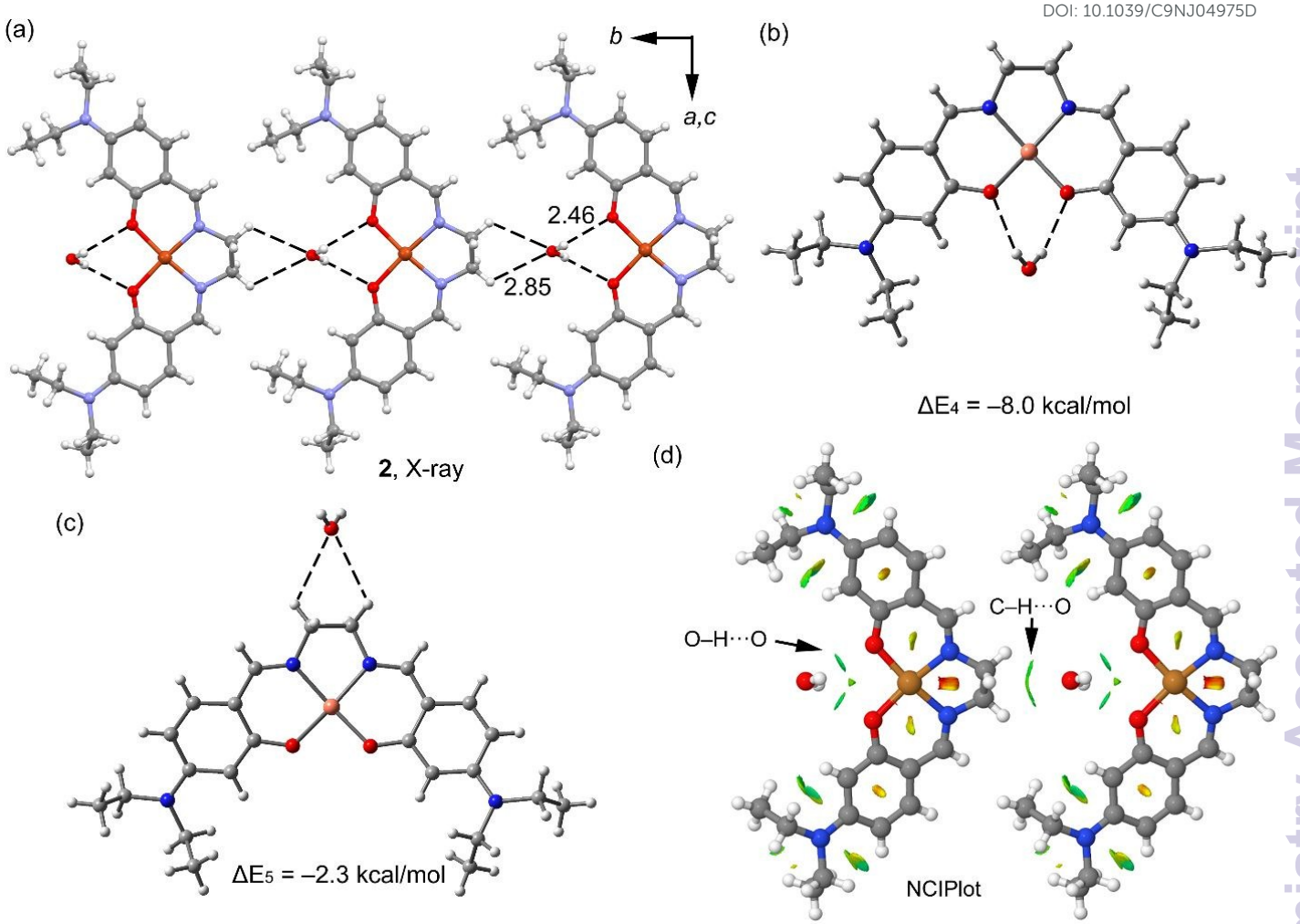

Fig. 6 (a) A section of the crystal structure (determined by X-ray structure analysis) of complex **2**. **(b,c)** Theoretical model used to compute the binding energy. Distances in Å. **(d)**. NCI plot of a dimeric fragment of the supramolecular chain in **2.** The gradient cut-off is s = 0.35 au, and the colour scale is −0.04 < ρ < 0.04 au.

3.6. Hirshfeld surface analysis

The Hirshfeld surfaces mapped over d_{norm} for compounds (***1***) and (***2***) are illustrated in Fig. 7. The Hirshfeld surface mapped over shape index property for (***2***) is shown in Fig. S6, ESI†. The surfaces are shown as transparent to allow visualization of molecules, around which they were computed. Red regions on the d_{norm} surface highlight the hydrogen bond acceptors and donors. The 2D fingerprint plots for all compounds (Fig. 8) illustrate the significant differences between the intermolecular interaction patterns. The dominant interaction in both compounds is the H···H interaction that comprise the 64.3 and 66.6% of the total Hirshfeld surface area of ***1*** and ***2***, respectively. The H···O/O···H intermolecular interactions are seen in d_{norm} surface plot of both compounds as white areas indicating that the distances of the C-H···O interactions are closer to the sum of the vdW radii. The proportion of the H···O/O···H contacts comprises 8.8 and 8.2% of the Hirshfeld surfaces for compounds ***1*** and ***2***, respectively. As was deduced previously, the supramolecular assembly of complex ***2*** includes chelate ring (CR)···π intermolecular interactions.

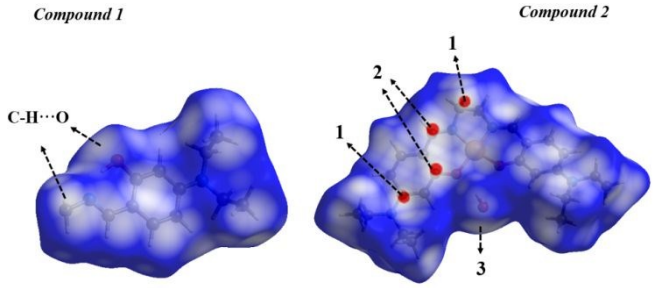

Fig. 7 Hirshfeld surfaces of compounds ***1*** and ***2*** mapped with d_{norm} function. Numbered arrows are discussed in the text.

These contacts are visible on the d_{norm} surface (Fig. 7) as bright red areas labelled 2. In addition, there are touching complementary pair of triangles in the shape index surface (Fig. S6, ESI†) indicating π-stacking interactions, as showed in the highlighted circles. C···C contacts attributed to π-stacking

View Article Online
DOI: 10.1039/C9NJ04975D

interactions are clearly identified in the fingerprint plots as a green area on the diagonal at approximately 1.8 Å (see Fig. 8). The fingerprint plots of both compounds as a pair of characteristic wings, typical for C-H···π interactions which comprise the 19.7 and 15.4% of the Hirshfeld surface area of ***1*** The red spots marked as 1 in the d_{norm} surface of complex (***2***) correspond to the presence of weak C-H···C interactions, including C-H···π contacts. The H···C/C···H contacts appear in ***1*** and ***2***, respectively. Analysis of decomposed fingerprint plots (**Fig. 8**) indicates that the most important types of interactions contributing to the crystal packing of both compounds are van der Waals forces (H···H contacts), weak hydrogen bonds (O···H), C-H···π contacts and π-stacking interactions.

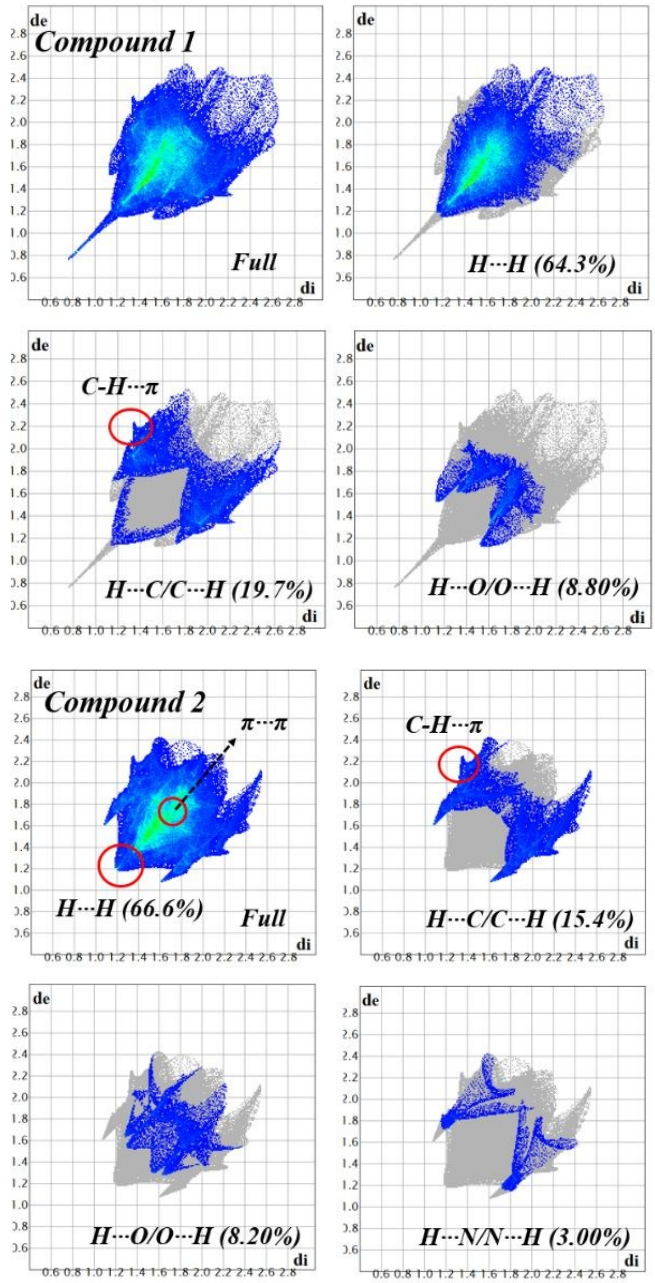

Fig. 8 Full and decomposed fingerprint plots for compound ***1*** (top) and compound ***2*** (bottom).

3.7. Antitumor properties

The antitumor properties of ligand (**1**), complex **2** and complex **3** were evaluated with the MTT assay in four different cancer cell lines in culture. The vanadyl complex did not show a cytotoxic effect against the tumour cell lines tested in the working concentration range (2.5-100 μM), except for MG-63 cells, whose viability was reduced to more than 50%. On the other hand, the copper complex outperformed the effect of the ligand exhibiting statistically significant effects: from 2.5 and 5.0 μM in MG-63 and MCF 7 cells, respectively, and from 10.0 μM for HT-29 and MDA-MB-231 cells ($p<0.001$). The ligand itself caused a similar cytotoxic effect only in MG-63 cells, and in HT-29 cell with a more pronounced effect than that observed for the vanadyl complex. Moreover, the IC_{50} values for the copper compound after a 24-hour treatment were 3.0, 3.6, 12.5 and 11.7 μM in MCF7, MG-63, MDA-MB-231 and HT-29 cells, respectively. These values turn out to be significantly lower than those obtained for cisplatin in the same cell lines: 42, 39, 131 and 120 μM, respectively.[43,44] These results are shown in Figure S7, ESI†.

Subin Kumar and coworkers reported the anticancer effects of novel copper-Schiff base ligand derived from vainillin showing an IC_{50} value around 50 μM on Dalton's lymphoma ascites cells. [45,46] In this sense, Creaven *et al*. reported a novel series of metal chelates with Schiff Bases ligands. Among all the ligands and metal complexes screened, copper complex showed the most potent activity (IC50 = 17.90 ± 3.75 μM), comparable to that of the clinical reference drug cisplatin (IC50 = 15.00 ± 2.65 μM) on hepatocarcinoma cells.[47]

Besides, pyridazine-based binuclear coppe(II) complexes with tridentate Schiff base ligands were active toward breast cancer cell line (MDA-MB-231) but also showed cytotoxicity on non tumoral cell line (L-6 myoblast) displaying a poor selectivity.[48] On the other hand, different mixed-ligand copper(II) Schiff base complexes exhibited an interesting anticancer activity showing the following range of IC50 values: 3-25 μM for Hela cells and 2-10 μM for HepG2 cells, respectively.[49]

In addition, it is interesting to note that many copper complexes with IC_{50} values in the submicromolar range has been identify as potent antitumor agents toward several human cancer cell lines.[50] Taking into account that complex ***2*** shows IC50 values in the range from 3 μM to 12 μM, it could be considered a promising non-platinum antitumor compound with remarkable cytotoxic effectiveness. So far, our findings indicate that the copper complex is an interesting candidate to be tested on *in vivo* models to demonstrate its efficacy as a novel compound in anticancer therapy.

4. Concluding Remarks

The synthesis and spectroscopic characterization of a macroacyclic Schiff base ligand and its mononuclear Cu(II) and VO(IV) complexes are reported. Complex (***2***) exhibits unconventional π···π(chelate ring) and H-bonding interactions in its solid state structure. Hirshfeld surface analysis was used to visualize intermolecular interactions in the crystal

structures. DFT calculations have been employed to explore the relative importance of these π(arene)–π(chelate ring) interactions using several computational tools. Moreover, the energetic analysis, including the estimation of contributions of the different forces (H-bonds and π-stacking), has been conducted using M06-2X/def2-TZVP calculations, and further corroborated with NCI plot index. The results allow us to conclude that the chelate ring···π interaction may be considered as a synthon interaction for the metal complex ***2***. The biological studies indicate that the copper complex is an interesting candidate to be tested on *in vivo* models to demonstrate its efficacy as a novel compound in anticancer therapy.

Acknowledgments

M.R. and D.M.G. thanks ANPCyT (PICT 2016-0226), A.L.D.V, I.E.L and M.C.R thanks ANPCyT (PICT 2016-1574) and SCAIT (Project D639/2) for financial support. A.F. thanks MINECO/AEI of Spain (project CTQ2017-85821-R FEDER funds) for financial support. We are also grateful to CTI (UIB) for computer allocation time. M.R. and M.C.R thanks CONICET for a fellowship.

References

1 C. A. Hunter and J. K. M. Sanders, *J. Am. Chem. Soc*., 1990, **112**, 5525–5534.
2 T. Steiner, *Angew. Chem. Int. Ed*., 2002, **41**, 48–76.
3 C. F. Matta, N. Castillo and R. J. Boyd, *J. Phys. Chem. B,* 2006, **110**, 563–578.
4 E. A. Mikhalyova, A. V. Yakovenko, M. Zeller, M. A. Kiskin, Y. V. Kolomzarov, I. L. Eremenko, A. W. Addison and V. V. Pavlishchuk, *Inorg. Chem*., 2015, 54, 3125–3133.
5 R. Rathore, S. H. Abdelwahed and I. A. Guzei, *J. Am. Chem. Soc*., 2003, **125**, 8712–8713.
6 M. Swart, T. van der Wijst, C. Fonseca Guerra and F. M. Bickelhaupt, *J. Mol. Model*., 2007, **13**, 1245–1257.
7 D. P. Malenov, G. V. Janjić, V. B. Medaković, M. B. Hall and S. D. Zarić, *Coord. Chem. Rev*., 2017, **345**, 318–341.
8 A. P. McKay, W. K. C. Lo, D. Preston, G. I. Giles, J. D. Crowley, J. E. Barnsley, K. C. Gordonv D. A. McMorran, *Inorg. Chim. Acta,* 2016, **446**, 41–53.
9 Y. P. Singh, R. N. Patel, Y. Singh, D. Choquesillo-Lazarte and R. J. Butcher, *Dalton Trans*., 2017, **46**, 2803–2820.
10 H. R. Masoodi, S. Bagheri and R. Ranjbar-Karimi, *Chem. Phys. Lett,*. 2017, **667**, 327–331.
11 W. Chen, G. Li and Y. He, *Phys. Chem. Chem. Phys*., 2014, **16**, 7907–7912.
12 E. R. T. Tiekink, *Coord. Chem. Rev*. 2017, 345, 209–228.
13 J. Qian, Q. Li, L. Liang, T. T. Li, Y. Hu and S. Huang, *Dalton Trans*., 2017, **46**, 14102–14106.
14 Q. Li, C. Han, M. Zhu, L. Yang, Y. Dong and J. Qian, *Inorg. Chim. Acta,* 2014, **461**, 298–300.
15 G. Romanowski and J. Kira, *Polyhedron*, 2013, **53**, 172-178.
16 K. C. Gupta, A. K. Sutar, *Coord. Chem. Rev.,* 2013, **252**, 1420.
17 I. Majunder, P. Chakraborty, R. Alvarez, M. González-Diaz, R. Peláez, Y. Ellahioui, A. Bauza, A. Frontera, E. Zangrando, S. Gómez-Ruíz and D. Das, *ACS Omega*, 2018, **3**, 13343-13353.
18 G. Barone, A. Terenzi, A. Lauria, A.M. Almerico, J.M. Leal, N. Busto and B. García, *Coord. Chem. Rev*. 2016, **257**, 2848.
19 P. Noblia, M. Vieites, B.S. Parajón-Costa, E.J. Baran, H. Cerecetto, P. Draper, M. González, O.E. Piro, E.E. Castellano, A. Azqueta, A.L. Cerain, A. Monge-Vega and D. Gambino, *J. Inorg. Biochem.* 2005, **99**, 443.
20 O. Güngör and P. Gürkan, *J. Mol. Struct*., 2014, 1074, 62.
21 A. Kathiravan, K. Sundaravel, M. Jaccob, G. Dhinagaran, A. Rameshkumar, D. Arul Ananth and T. Sivasudha, *J. Phys. Chem. B,* 2014, **118**, 13573–13581.
22 W. Al Zoubi, A. A. S. Al-Hamdani, M. Kaseem, *Appl. Organometal. Chem,*. 2016, **30**, 810-817.
23 M.M. Rahman, T.A. Sheikh, R.M. El-Shishtawy, M.N. Arshad, F.A.M. Al-Zahrani, A.M. Asiri, *RSC Adv.,* 2018, **8**, 19754-19764.
24 CrysAlisPro, Oxford Diffraction Ltd., version 1.171.33.48 (release 15-09-2009 CrysAlis171.NET).
25 *(a)* G. M. Sheldrick, Acta Cryst., 2015, **A71**, 3–8; *(b)* G. M. Sheldrick, *Acta Cryst*. 2008, **A64**, 112-122.
26 (*a*) M. A. Spackman& D. Jayatilaka, *CrystEngComm*, 2009, 11, 19–32; (*b*) J. J. McKinnon, D. Jayatilaka, M. A. Spackman, *Chem. Commun.,* 2007, 3814-3816.
27 S. K. Wolff, D. J. Grimwood, J. J. McKinnon, M. J. Turner, D. Jayatilaka, M. A. Spackman, (2012). CrystalExplorer3.0, The University of Western Australia.
28 Gaussian 09, Revision C.02, M.J. Frisch, G.W. Trucks, H.B. Schlegel, G.E. Scuseria, M.A. Robb, J.R. Cheeseman, G. Scalmani, V. Barone, G.A. Petersson, H. Nakatsuji, X. Li, M. Caricato, A. Marenich, J. Bloino, B.G. Janesko, R. Gomperts, B. Mennucci, H.P. Hratchian, J.V. Ortiz, A.F. Izmaylov, J.L. Sonnenberg, D. Williams-Young, F. Ding, F. Lipparini, F. Egidi, J. Goings, B. Peng, A. Petrone, T. Henderson, D. Ranasinghe, V.G. Zakrzewski, J. Gao, N. Rega, G. Zheng, W. Liang, M. Hada, M. Ehara, K. Toyota, R. Fukuda, J. Hasegawa, M. Ishida, T. Nakajima, Y. Honda, O. Kitao, H. Nakai, T. Vreven, K. Throssell, J.A. Montgomery, Jr., J.E. Peralta, F. Ogliaro, M. Bearpark, J.J. Heyd, E. Brothers, K.N. Kudin, V.N. Staroverov, T. Keith, R. Kobayashi, J. Normand, K. Raghavachari, A. Rendell, J.C. Burant, S.S. Iyengar, J. Tomasi, M. Cossi, J.M. Millam, M. Klene, C. Adamo, R. Cammi, J.W. Ochterski, R.L. Martin, K. Morokuma, O. Farkas, J.B. Foresman, D.J. Fox, Gaussian, Inc., Wallingford CT, 2016.
29 (a) U. Saha, D. Dutta, H. Nath, A. Franconetti, A. Frontera and M. K. Bhattacharyya, *Inorg. Chim. Acta*, 2019, **488**, 159-169; (b) M. S. Gargari, V. Stilinović, A. Bauzá, A. Frontera, P. McArdle, D. Van Derveer, S. W. Ng and G. Mahmoudi, *Chem. Eur. J*., 2015, **21**, 17951–17958; (c) M. Mirzaei, H. Eshtiagh-Hosseini, Z. Bolouri, Z. Rahmati, A. Esmaeilzadeh, A. Hassanpoor, A. Bauza, P. Ballester, M. Barceló-Oliver, J. T. Mague, B. Notash and A. Frontera, *Cryst. Growth Des*., 2015, **15**, 1351-1361; (d) S. Mirdya, S. Roy, S. Chatterjee, A. Bauzá, A. Frontera and S. Chattopadhyay, *Cryst. Growth Des*., 2019, **19**, 5869-5881.
30 S. B. Boys, F. Bernardi, *Mol. Phys*., 1970, 19, 553–566.
31 J. Contreras-García, E. R. Johnson, S. Keinan, R. Chaudret, J.-P. Piquemal, D. N. Beratan and W. Yang, *J. Chem. Theory Comput.*, 2011, **7**, 625-632.
32 E.R. Johnson, S. Keinan, P. Mori-Sanchez, J. Contreras-Garcia, A.J. Cohen and W. Yang, *J. Am. Chem. Soc.,* 2010, **132**, 6498-6506.
33 T. Mosmann. *J. Inmunol.* 1983, **65**, 55-63.
34 S. Khan, S. Sproules, L. S. Natrajan, K. Harms and S. Chattopadhyay, *New J. Chem*. 2018, **42**, 1634-1641.
35 S. Khan, A. A. Masum, M. M. Islam, M.G.B. Drew, A. Bauzá, A. Frontera and S. Chattopadhyay*, Polyhedron*, 2017, **123**, 334-343.
36 U. Singh, M. M. Dar, S. Anayutullah, H. Alam, N. Manzoor, S. A. Al-Thabaiti and A. A. Hashmi, *J. Coord. Chem*., 2015, **68**, 2096-2106.
37 A. Bhattacharyya, A. Bauzá, S. Sproules, L. S. Natrajan, A. Frontera and S. Chattopadhyay, *Polyhedron*, 2017, **137**, 332–346.

View Article Online
DOI: 10.1039/C9NJ04975D

38 S. Khan, S. Jana, M. G. B. Drew, A. Bauza, A. Frontera and S. Chattopadhyay, *RSC Adv*., 2016, **6**, 61214–61220.
39 S. Khan, P. Giri, A. Bauza, K. Harms, A. Frontera and S. Chattopadhyay, *Polyhedron*, 2019, **157**, 487-494.
40 G. Mahmoudi, J. K. Zareba, A. Bauza, M. Kubicki, A Bartyzel, A. D Keramidas, L. Butusov, B. Miroslaw and A. Frontera, *CrystEngComm*., 2018, **20**, 1065-1076.
41 F. A. Afkhami, A. K. Khandar, G. Mahmoudi, W. Maniukiewicz, A. V. Gurbanov, F. I. Zubkov, O. Sahin, O. Z. Yesilel and A. Frontera, *CrystEngComm*., 2017, **19**, 1389-1399.
42 S. J. Grabowski, *Chem. Rev*. 2011, **111**, 2597-2625.
43 M. C. Ruiz, J. Kljun, L. Turel, A. L. Di Virgilio and I. E. León, *Metallomics*, 2019, 11, 666-675.
44 L. H. Swift and R. M. Golsteyn. *Biol. Cell.* 2016, **108**, 127-148.
45 K. Subin Kumar and K. K. Aravindakshan, *J. Pharm. Chem. Biol. Sci.* 2017, **5**, 271-281.
46 K. Subin Kumar, C. Priya Varma, V. N. Reena and K. K Aravindakshan, *J. Pharm. Sci. & Res.,* 2017, **9**, 1317-1323.
47 B.S. Creaven, B. Duff, D.A. Egan, K. Kayanagh, G. Rosair, V. Reddy and M. Walsh. *Inorg. Chim. Acta*, 2010, **363**, 4048-4058.
48 U. M. Rafi, D. Mahendiran, A.K. Haleel, R.P. Nankar, M. Doble and A. K. Rahiman, *New J. Chem*., 2016, **40**, 2451-2465.
49 W. J. Lian, X. T. Wang, C. Z. Xie, H. Tian, X. Q. Song, H. T. Pan and X. Qiao, *Dalton Trans*. 2016, **45**, 9073-9087.
50 C. Santini, M. Pellei, V. Gandin, M. Porchia, F. Tisaato and C. Marzano, *Chem. Rev*., 2014, **114**, 815-862.

View Article Online
DOI: 10.1039/C9NJ04975D

A combined experimental and theoretical study and cytotoxicity assays of diethylaminophenyl-based Schiff base Cu(II) and VO(IV) complexes is reported. Cu(II) complex shows interesting chelate ring···π interactions in the crystal structure